Multispectral Remote Sensing and Truth Data from the *Tenyo Maru* Oil Spill*

Abstract

On 22 July 1991, the Tenyo Maru *sank in 87 fathoms of water off Cape Flattery, Washington following a collision with the grain ship* Tou Hai. *The initial spill included approximately 100,000 gallons of the bunker oil and diesel fuel carried by the* Tenyo Maru. *Oil continued to be released at a rate of approximately 500 gallons per day during the subsequent weeks. Sea-truth and remote sensing data were collected in the vicinity of the wreck site during the period 5–10 August 1991. Oil content in samples representing 150 cm² of ocean surface typically ranged from undetectable to 180 mg. Most samples contained 5 mg of oil or less, indicating an oil film less than 0.5 micrometres thick at these locations. Chemical analysis of samples identified two unique oils in the slick, one containing enhanced concentrations of toxic PAH. The remote sensing data revealed variability in oil thickness, particularly through the ultraviolet and long-wave infrared bands and, secondarily, in other visible and near-infrared bands. Processing is described to remove atmospheric effects from the remote sensing data and combine ultraviolet and infrared band data into a single intuitive display. A mid-wave infrared band showed no useful signature for the oils present at Neah Bay. No microwave signature was observed due to the small oil amounts.*

Introduction

During the period 5–10 August 1991, multispectral data (Smith, 1991; Rogne and Smith, 1992) were collected over an oil slick in the open ocean and verified with oceanographic and chemical collections (MacDonald, 1991; Texas A&M, 1992). This paper summarizes analysis of the multispectral data and comparison of remote sensing with sea-truth observations.

The goals of this experiment were to use the Neah Bay as a case study to examine

- the utility of two readily available multispectral sensors for oil detection;
- the relative utility of spectral bands (in addition to commonly used ultraviolet and infrared bands) to detect and characterize spilled oil; and
- the image processing and image understanding requirements for reliable detection and characterization of spilled oil.

In support of these goals, the following data were collected and analyzed;

- multispectral imagery, including up to 16 spectral bands in the ultraviolet through thermal infrared;
- C- and Ka-band microwave radiometer measurements; and
- sea-truth measuring surface oil amounts and composition.

Special features of this case study include broad spectral coverage in the remote sensing data, the uncontrolled nature of the spill, and the coordination with oceanographic collections.

Sea-Truth Sampling

Sea-truth sample data were collected from chartered sport fishing boats on 5, 6, and 10 August 1991. Two types of samples were collected: wipe samples of surface oil, and water samples taken 0.5 m beneath the surface. Wipes were collected at, minimally, 0.1-nm intervals along remote sensing flight-lines–more frequently if a variety of slick forms (e.g., mousse and floating tar balls) were present. Collections were also made at points where no visible oil was present. During collection, a 5- by 30-cm strip of Nytex mesh was secured to the end of a 2.5-m aluminum pole. Both clamp and strip were thoroughly rinsed with methylene chloride prior to collection. The strip was then gently placed on the water surface so that the floating slick would adhere to it, carefully retrieved to avoid contamination, and stored chilled in a clean (to EPA standards) 60-ml jar. Brief descriptions of the slick were recorded in a log for all collections. During the 10 August cruise, collection of each wipe sample was recorded on video tape annotated with both oral descriptions and time overprint. Care was taken to sample from the up-wind side of the boat and to extend the pole well beyond the boat's hull before placing the strip on the water.

Flagged drogue bouys to which were attached 4-foot square pieces of foil-covered hard foam were used as markers to establish remote sensing flight lines correlated with sea-truth sampling lines. The flags were effective in allowing the boat crews to relocate the buoys. The foil squares were intended to increase buoy visibility from the air and provide a marker in the remote sensing data. In practice, visibility from the air was marginal at best, and no marker was unambiguously identified in the remote sensing data.

Water-column samples were liquid-liquid extracted with

*Presented at the First Thematic Conference on Remote Sensing for Marine and Coastal Environments, New Orleans, Louisiana, 15-17 June 1992.

Timothy Rogne
Environmental Research Institute of Michigan, P. O. Box 134001, Ann Arbor, MI 48113-4001.

Ian MacDonald
Geochemical & Environmental Research Group, Texas A&M University, 833 Graham Road, College Station, TX 77845.

Alexandra Smith
Environmental Research Institute of Michigan, P. O. Box 134001, Ann Arbor, MI 48113-4001.

M. C. Kennicutt II
Geochemical & Environmental Research Group, Texas A&M University, 833 Graham Road, College Station, TX 77845.

Charles Giammona
Marine Spill Response Corporation, 1350 I Street NW, Suite 300, Washington, DC 20005.

Photogrammetric Engineering & Remote Sensing, Vol. 59, No. 3, March 1993, pp. 391–397.

0099-1112/93/5903–391$03.00/0

methylene chloride using Geochemical Environmental Research Group (GERG) standard operating procedures. Extracts were concentrated and weighed with an electrobalance. Water extracts were screened by gas chromatograph with flame ionized detection (GC/FID) and polynuclear aromatic hydrocarbons (PAH) were quantified by gas chromatography/mass spectrometry/selected ion monitoring (GC/MS/SIM). Wipe samples and beach tar samples were extracted with methylene chloride, concentrated, and weighed by electrobalance. Samples were screened by GC/FID, and selected samples were analyzed for PAH content by GC/MS/SIM. Other slick extracts were analyzed for quantitative biological markers.

Remote Sensing Data Collection

Remote sensing data were acquired with two sensor/platform combinations: A Modular Multi-Band Scanner (M²S) mounted on a Volpar Beech BE-8T aircraft, and a de Havilland Caribou aircraft mounting the M7 multispectral scanner and two microwave radiometers (Smith, 1991). Only the M7 multispectral scanner data are considered in this paper.

The M7 (Figure 1) is a line scanning sensor imaging a 90-degree field-of-view beneath the aircraft at 2.5 milliradian resolution in 16 spectral bands. At Neah Bay, the aircraft was flown at 1000- and 3900-foot altitudes, providing nadir pixel footprints measuring 0.8 and 3 metres, respectively. The sensor is not stabilized; an Inertial Navigation System (INS) provides data to correct for aircraft motion in post-processing. A LORAN receiver provided position reference for the remote sensing data.

As part of standard processing, multispectral scanner data were transferred to CCT, screened for data corrupted during the recording and playback process, registered, corrected for aircraft roll and pitch, and resampled to a uniform spatial grid on the ocean. The experiment-specific processing included normalization for atmospheric effects, comparison of signatures with truth observations, and preparation of composite images to highlight oil features.

Normalization proved necessary for the ultraviolet and visible band data where signature variations caused by path radiance and directional reflectance effects often exceeded the oil/water contrast. Clear water data, chosen to be relatively free of sun glint, were used to estimate systematic variations in the local mean signature that were uncorrelated with ocean surface characteristics. The LOWTRAN 7 model (Kneizys, 1988) was used to estimate atmospheric transmission loss between the sensor platform and the ocean in each spectral band as a function of scan angle. Appendix A provides a prescription for the normalization procedure. The procedure is designed to provide accurate contrast signatures (e.g., the signature difference between sheen and water) within and between scenes, but does not attempt to preserve absolute signal levels.

Comparison of signatures with truth observations was complicated by difficulties in spatially correlating the samples. Marker buoys and reflective panels were ineffective. The LORAN data accuracy was insufficient to mark sample and remote sensing pixel locations within the scale of slick variations (on the order of tens of metres). In practice, we used the observed sea-truth boat location (using aerial photography to provide boat identification) in the remote sensing imagery to provide a reference point in space and time, and the boat's wake scar to constrain its path. The boat track derived from LORAN data was forced to fit the observed scar; sample locations were assigned to the path based on the sample time and the constrained track. In all, data from three aircraft passes could be correlated with ten sample locations. Of these, six sample positions could be located along a wake scar, while four had to be extrapolated from the boat track observed at the time the imagery was collected.

Three procedures were used to form image composites from the normalized multispectral data: a phenomenologically motivated technique based on the expected behavior of UV (ultraviolet) and IR (infrared) oil/ocean signatures, RGB-mapped display of selected bands forming "natural color" images, and composites formed from linear transformations of the spectral data.

The utility of UV and IR signatures in oil remote sensing is well known (e.g., Horvath, 1971; Horvath, 1974; Fingas,

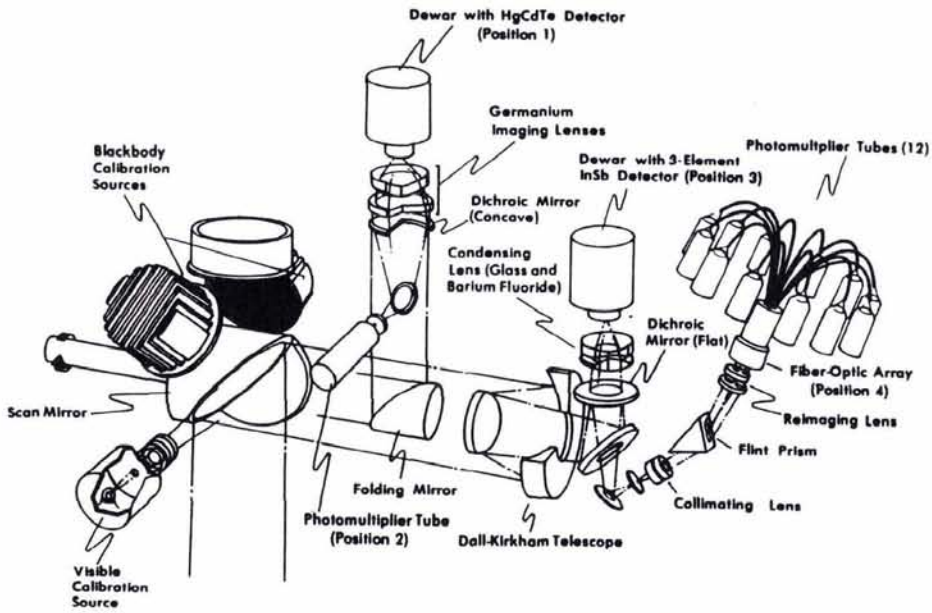

M7 Spectral Bands	
Channel	50% Response (μm)
1	0.357 - 0.381
2	0.414 - 0.433
3	0.439 - 0.460
4	0.466 - 0.485
5	0.494 - 0.531
6	0.540 - 0.585
7	0.592 - 0.634
8	0.646 - 0.723
9	0.811 - 0.938
10	0.910 - 1.015
11	1.230 - 1.296
12	1.560 - 1.665
13	2.012 - 2.290
14	3.383 - 5.380
15	9.380 - 11.590
16	7.170 - 12.110

Figure 1. Optical diagram of the M7 scanner.

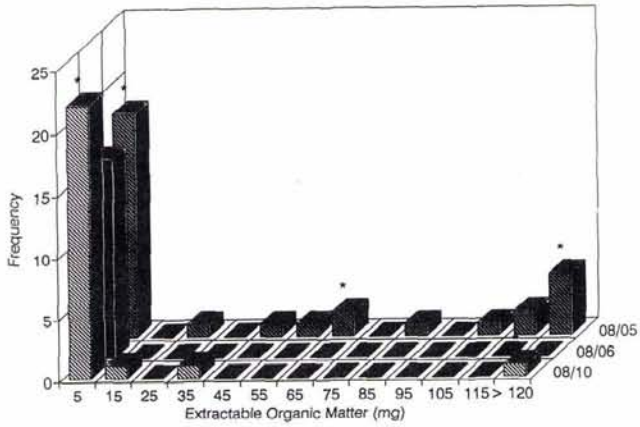

Figure 2. Distribution of sample weights from slick samples collected during three days of sea-truth operations.

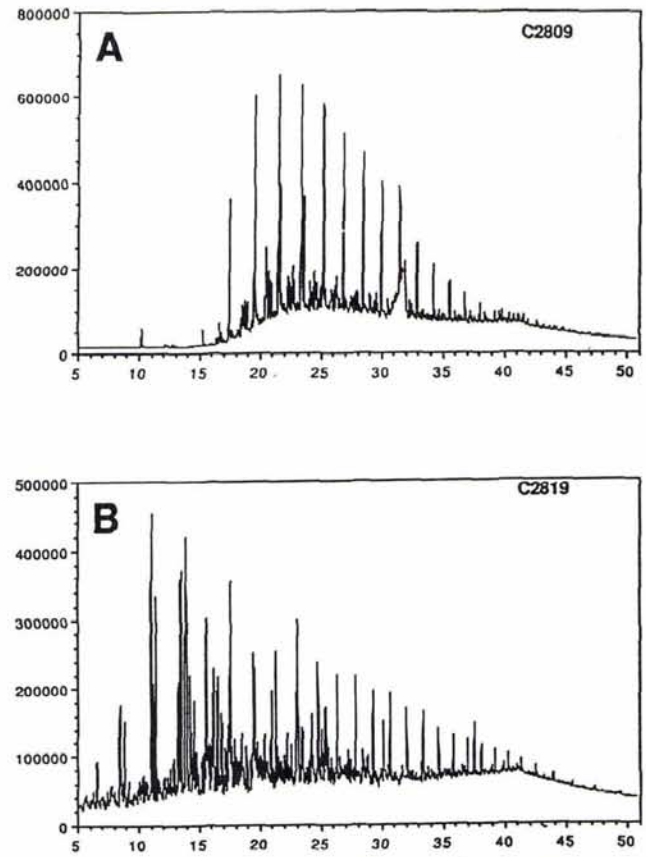

Figure 3. Gas chromatograph fingerprints for the two types of oil detected in the slick.

1991). Because positive contrast UV signatures are produced for very thin sheens while thicker oil is required to support an IR signature, a composite of these bands is a natural way to segragate heavier oiled regions from very thin sheen. In addition, correlating the presence of UV and IR signatures aided in rejecting signatures not associated with oil (e.g., thermal scars from recovery vessel traffic). A presciption for producing them is provided in Appendix B.

Natural color composites were produced mapping M7 channels 3, 5 or 6, and 8 to blue, green, and red display colors, respectively. These composites were produced because correlations between slick characteristics and color are also well known (e.g., National Research Council, 1985).

The third class of composites was formed from spectral features. A feature is an algebraic combination of spectral data that correlates with a scene property of interest. The goal is to extract desirable information from a high dimension data space (e.g., the 16 M7 channels) and form a low dimension data space composed of a few features that is more amenable for display and interpretation. Two techniques were used to define the weights for combining bands into features: the Gram-Schmidt procedure [Jackson, 1983] for generating orthogonal features based on spectra measured from interesting scene components (e.g., sheen, clear water, thicker oil), and the principal component method.

TABLE 1. SUMMARY OF SEA-TRUTH SAMPLE DATA CORRELATING WITH 10 AUGUST REMOTE SENSING DATA

Sample #	Run #	Oil Type	Weight (mg)	Equivalent Thickness(μm)	Description
W81	(5)*	--	0.2	---	Few broken slick droplets
W82	(5)*	--	0.1	---	No visible slick
W85	5	--	0.2	---	No visible slick
W86	5	--	0.2	0.01	Sheen
W87	5	2	183.2	12.2	Oil rising to surface, fresh oil glob
W89	8	2	9.9	0.7	Rainbow sheen, mousse, fresh oil glob
W94	12	--	0.4	---	Light mousse
W95	12	1	34.6	2.3	Heavy slick with patches of floating tar and silver sheen
W96	12	1	0.6	0.04	Silver sheen, patches of tar
W97	12	1	18.2	1.2	Floating tarball
W98	12	--	0.3	---	No visible oil
W99	12	--	0.2	---	No visible oil

*Exact sample locations cannot be identified

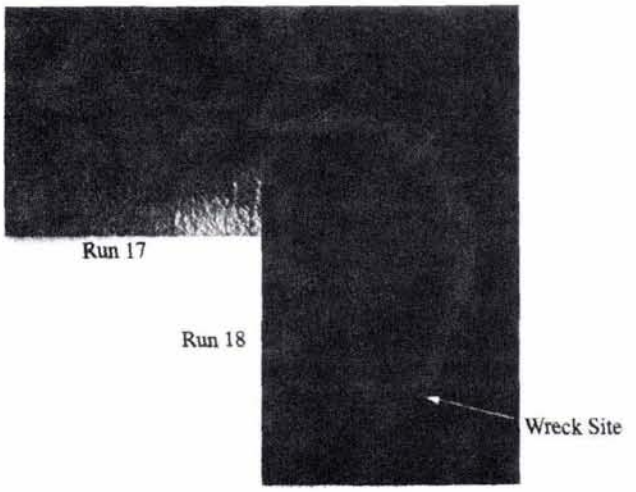

Figure 4. Composite of UV band data from Runs 17 and 18 showing an overview of the slick studied.

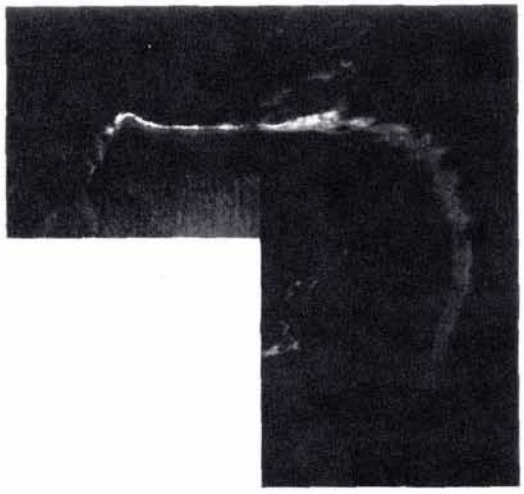

Figure 6. UV/IR composites for Runs 17 and 18.

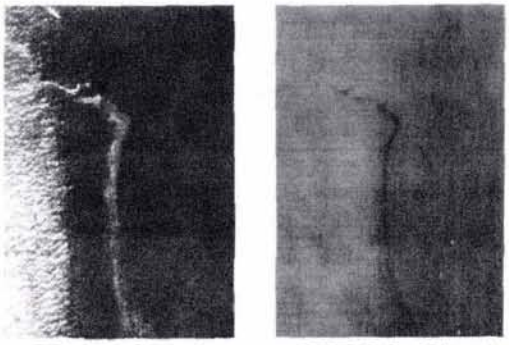

Figure 5. UV and LWIR band data for Run 18.

throughout the sampling period suggests that two discrete sources of leakage were present on the sunken ship.

Six tar samples collected in a very limited beach survey were analyzed. All samples contained detectable hydrocarbons, but only one had high levels of PAH contamination. Interestingly, biological marker compositions indicate that the *Tenyo Maru* was the source of this sample, while eliminating the *Tenyo Maru* as the source of the other samples. In particular, five of the beach extracts contained oleanane and a peak tentatively identified as gammacerane. The *Tenyo Maru* slicks contain neither of these compounds. Likewise, the *Tenyo Maru* slick contained tricyclic triterpanes, which were absent from the five samples. The beach sample with the highest level of fresh oil contained tricyclic triterpanes, but lacked oleanane and gammacerane.

The sea-truth information used to correlate with remote sensing observations were wipe sample weight and composi-

Sea-Truth Sampling Results

The highest hydrocarbon concentrations observed in the water column samples were from samples collected directly beneath the visible slick, where total PAHs reached 2360 ng/l. Wipe samples of the slick provided a semi-quantitative estimate of the amount of oil on the sea surface. Localized high values in the areas of high oil volume illustrate the heterogeneity of the slick distribution and the consistent pattern of comparatively light and heavy oil on all three sampling days (Figure 2). A few of the slick samples (5 August) contained several grams of oil. The majority of samples contained 5 mg of oil or less, which corresponds to a very thin (<0.5 μm) film over the sample area.

Oil "fingerprints" (GC/FID) demonstrated that two distinct oil types were present in the slick emanating from the ship (Figure 3). One fluid (**A**) was predominantly normal alkanes typical of diesel fuel whereas the other fluid (**B**) was enriched in polycyclic aromatic compounds, particularly lower molecular weight compounds. No known physical, chemical, or biological process will produce such distinct fingerprints from a single source. Observations of the two fingerprints

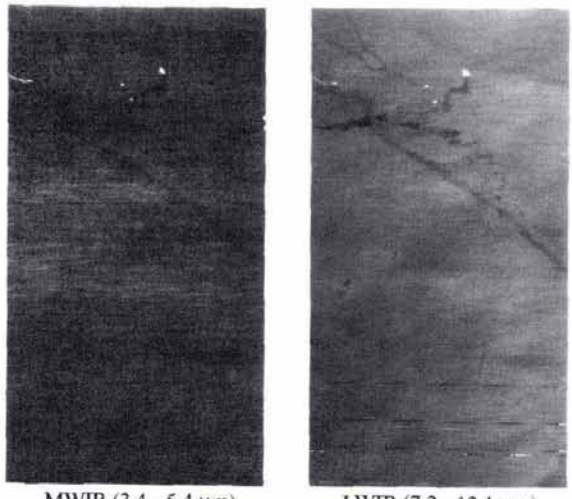

Figure 7. MWIR and LWIR band data for Run 18.

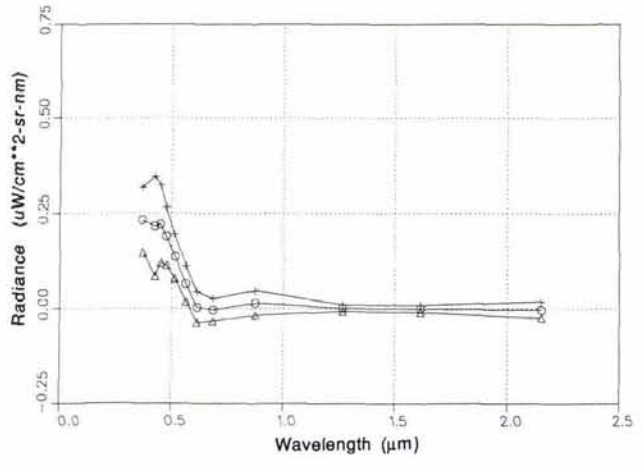

(a)

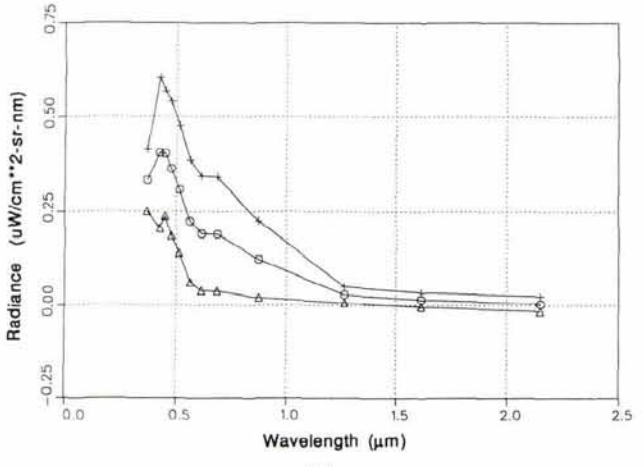

(b)

Figure 8. Differential radiance of two oiled areas relative to clear water, (a) sheen, (b) thicker oil.

tion from the 10 August collection. Table 1 summarizes the relevant data. For reference, the sample weights are translated into an equivalent slick thickness, assuming a uniform oil distribution over the 150 cm² sample area. Clearly, a relatively thin slick was observed. Run numbers in Table 1 refer to remote sensing data sets in which the sample locations are observed.

Remote Sensing Results

The highest quality remote sensing data correlated with sea-truth were collected on 10 August; these data were used for all analyses (Rogne and Smith, 1992). On the afternoon of the 10th the main slick was observed extending approximately 2 km north from the wreck site, and then extending west for approximately 3 km (Figure 4). The turn west corresponds to the presence of a cold water mass observed in the IR data. The northern oil motion was wind-driven while the turn west was apparently caused by entrainment in a local current.

The total slick area, as observed in the UV imagery, covered approximately 450,000m². A strong negative contrast infrared signature was observed along the east/west portion of the slick; presumably the slick thickened in this region due to containment of wind-driven oil along the thermal boundary. These slick areas covered approximately 100,000m².

Interestingly, neither the aircraft team or the sea-truth team were aware of the oceanographic front and its effect on the oil dispersion during sampling operations. The sea-truth team followed the wind-driven plume north from the wreck site and did not sample the (apparently) thicker oil in the western arm of the slick. The aircraft crew saw the thicker oil along the east/west slick arm and assumed that the wreck site was at the western end of this arm (rather than at its true location at the southern end of the north/south arm).

Normalized (atmosphere-corrected) imagery from UV and LWIR (Long-Wave Infrared) bands is shown in Figure 5. The images represent an area measuring approximately 3.5 by 2.2 km showing the wind-driven plume arm and part of the current-driven arm; the oil source and wreck site are located near the bottom of the images. Note the wake scars from recovery vessel traffic in the LWIR band image, and the negative contrast oil signature seen where the plume turns west. UV/IR composites (Figure 6) show both arms of the slick. This composite is normally produced in color with red assigned to the processed IR data and cyan assigned to the processed UV data. The black-and-white version shown assigns the IR data to bright tones and the UV data to the dimmer gray levels. The composite processing rejects the wake scars and focuses attention on the oil features. Severe sun glint which saturated portions of the data (e.g., Run 17) was not rejected by the processing. The IR data indicates that the heaviest oil concentrations are along the northern edge of the east/west slick section. This correlates with the visual appearance of the slick.

Figure 7 compares LWIR and MWIR (Mid-Wave Infrared) band data. While wake scars are clearly evident in both bands, and a strong oil signature is present in the LWIR band, no significant oil signature is seen in the MWIR band.

Image composites based on "natural color" band combinations were effective in showing color differences between what is believed to be thicker oil in the east/west slick arm and sheen in other slick areas. However, when composites based on spectral features were prepared, oil features were dominated by the UV and LWIR band data with only secondary contributions from visible wavelength bands. The other bands were effective in discriminating sun glint and other scene objects such as recovery vessels.

Figure 8 shows samples of mean spectra (computed from collections of 50 to 100 pixels) contrasting clear water, sheen, and "thicker oil" computed from normalized data over the north/south slick arm. The signature difference between oil and clear water areas is plotted. Bounds about the mean indicate the 2σ variation among the individual pixels. Data are plotted for the UV, visible, near-IR, and shortwave-IR M7 bands (see Figure 1 for bandpasses). The sheen spectra reflect the bright, bluish appearance of this oil compared to the increased red content of the thicker oil.

Conclusions

The main results from the remote sensing data analyses are as follows:

- Normalization procedures were successfully applied to remove unwanted atmospheric effects from the remote sensing data.
- Confirming well-known empirical and theoretical results, the ultraviolet (UV) spectral channel provided excellent detection of the slick boundary (including very thin sheen), while the long-wave infrared (LWIR) channel (7.2 to 12.1 μm) provided selective response to thicker oil films.

- Due to the thin oil films at Neah Bay, only negative contrast infrared signatures were observed; signatures magnitudes suggest both evaporative cooling and reduced emissivity contributed to the oil signature.
- For the oil observed at Neah Bay, the mid-wave infrared (MWIR) channel (3.4 to 5.4 μm) did not reveal an oil signature, though thermal scars from vessel traffic were clearly visible.
- Inspection of complete spectra for different slick components (sheen, thicker oil, and areas containing oil with the two compositions observed) showed the well-known color variations of oil films as a function of thickness; no evidence for separating the two oil compositions was found.
- Processing based on phenomenological arguments using the UV and LWIR bands produced good composites highlighting oil features and rejecting clutter observed in the individual channels.
- Composites formed from a selection of UV, visible, near-IR, and LWIR bands improved discrimination of non-oil image features (sun glint, vessels, aircraft) but did not add significant oil feature information.
- Due to the small size and thinness of the slick, no microwave oil signature was observed.

Results related to the sea-truth data include

- Sea truth data confirmed oiled versus clear water areas observed in the remote sensing data, but did not sample areas thought to contain the thickest oil.
- Samples covering 150 cm^2 typically contained 0 to 180 mg of oil, but the majority of slick samples contained 5 mg of oil or less. A few samples contained several grams of oil.
- Chemical analysis revealed two distinct oils.
- Limitations in georeferencing of sea-truth and remote sensing data limited the opportunities for comparison.
- Field-expedient markers intended to identify sea-truth sample locations in the remote sensing data were ineffective.
- Direction of sea-truth sampling from the remote sensing platform was not successful, primarily due to limitations in position information.
- The small spatial scale and infrequency of sea-truth samples compared to remote sensing pixels can make direct comparisons difficult (e.g., an isolated tarball can dominate the character of a sea-truth sample, but be an insignificant component of a remote sensing pixel).
- Future studies of this type require sea-truth that fully characterizes conditions over the scale of a few remote sensing pixels, allows spatial referencing of the data within this scale, and is directed by characteristics observed in the remote sensing data.

Care must be taken in drawing conclusions from this study regarding the use of multispectral sensors for oil characterization in an operational setting. Virtually all the oil observed formed a very thin surface film which was measured during the day. This biased toward the success of UV/LWIR channels and against the success of the microwave radiometers (or the importance of other multispectral channels). We did show that

- Image composites allowing straightforward interpretation of oil characteristics can be formed with relatively simple processing, readily implemented in real time.
- Preparation of composites can be performed prior to geometric resampling and georeferencing; georeferencing a derived product (e.g., a slick contour) greatly reduces the computational load.
- Successful remote sensing requires a stable sensor/platform configuration (e.g., to insure adequate georeferencing, proper spectral bands, and adequate response time).
- Weather is an important factor to consider when engineering an operational sensor/platform combination.

Recommendations

These recommendations pertain most directly to a subsequent exercise designed to correlate remote sensing and sea-truth data of an uncontrolled spill:

- A more dense sea-truth sample grid is required.
- Sea-truth must be representative of slick inhomogeneities (e.g., mixtures of sheen and tarballs) within scales on the order of remote sensing pixels.
- The remote sensing platform should be able to specify sea-truth sample locations based on the observed oil distribution.
- Better (visible) sample markers and/or better georeferencing (on the order of 10 metres for slick variations observed at Neah Bay) is required to reliably correlate remote sensing data with sample locations.
- An operations plan should be developed prior to conducting further field experiments at a "spill of opportunity."
- Controlled experiments should be considered to test the operations plan.

References

Fingas, Merv, 1991. The Technology of Oil Spill Remote Sensing, *U.S. Coast Guard Oil Spill Remote Sensing Workshop*, ERIM Report #213259.

Horvath, R., 1974. *Interpretation Manual for the Airborne Remote Sensor System*, ERIM Report #CG-250-44.

Horvath, R., W.L. Morgan, and S.R. Stewart, 1971. *Optical Remote Sensing of Oil Slicks: Signature Analysis and Systems Evaluation*, University of Michigan Willow Run Laboratories, Report #724104.2/1.

Jackson, Ray D., 1983. Spectral Indices in N-space, *Remote Sensing of Environment*, 13:409–421.

Kneizys, F.X., E.P. Shettle, G.P. Anderson, L.W. Abreu, J.H. Chetwynd, J.E.A. Selby, S.A. Clough, and W.O. Gallery, 1988. *Users Guide to LOWTRAN 7*, U.S. Air Force Geophysics Laboratory, AFGL-TR-88-0177.

MacDonald, Ian, 1991. *Spectral Signature Characterization and Sea-Truth of the* Tenyo Maru *Oil Spill*, Texas A&M University Geochemical and Environmental Research Group (GERG) Field Report.

National Research Council Commission on Physical Sciences, Mathematics, and Resources, 1985. *Oil in the Sea*, National Academy Press.

Rogne, T.J., and A.M. Smith, 1992. Tenyo Maru *Oil Spill Remote Sensing Data Analysis*, Environmental Research Institute of Michigan Report #239400-6-T.

Smith, A.M., 1991. Tenyo Maru *Oil Spill, Neah Bay Remote Sensing Collection*, Environmental Research Institute of Michigan Report #239400-3-T.

Texas A&M University Geochemical and Environmental Research Group (GERG), 1992. Tenyo Maru *Oil Spill, Data Synthesis*, Technical Report #92-056.

Appendix A

Normalization Procedure

The normalization algorithm applied to the Neah Bay data is

(1) Identify an area of clear water, homogeneous in appearance, along the current flight line.
(2) Average a group of scan lines to suppress the impact of isolated glints or anomalies.
(3) Fit the scan angle dependence of the averaged radiance signal to a low-order polynomial (L') to further suppress the impact of isolated glints or anomalies.
(4) Run LOWTRAN 7 to estimate atmospheric transmission in each spectral band (T) as a function of scan angle.
(5) Apply normalization formula with derived path radiance dependence to the entire scene.

The correction formula in a single spectral band is derived as follows:

$$L'(\theta) = L_w T(\theta) + L_p(\theta) \qquad L(\theta) = L_n(\theta)T(\theta) + L_p(\theta)$$

Solving for L_n and substituting for L_p we find

$$L_n(\theta) = L(\theta)/T(\theta) - [(L'(\theta) - L_w T(\theta))/T(\theta)]$$

where L_n is the normalized measurement, L is the original measurement, T is the estimated atmospheric transmission from LOWTRAN, L_w is the (assumed) diffuse radiance of the ocean observed for the clear water data (fit to $L'(\theta)$), L_p is the path radiance, and θ is the scan angle. As applied to the Neah Bay data, we equated L_w with the nadir measurement over clear water ($L'(\theta)$). Thus, scan angle variations within a scene have been removed, but a bias signal equal to the nadir view path radiance remains. Scaling for illumination variations was not necessary at Neah Bay, but must be accounted for in the general case.

Appendix B

UV/IR Composite Prescription

In the Neah Bay case, the production and interpretation of UV/IR composites is simplified by the fact that only negative contrast thermal signatures were observed. This was most likely due to the relatively small oil amounts (relatively thin slick) and the fresh, volatile nature of the material. Thus, a simple algorithm was followed to automatically produce the composites. The algorithm is

(1) Measure mean clear water signal and subtract from the UV image.
(2) Create a UV display image spanning 0 to 0.3 $\mu W/cm^2$-sr-nm (black to white) and apply an erosion operator.
(3) Invert IR image.
(4) Measure clear water mean signal and subtract from IR image.
(5) Measure standard deviation of UV image clear water signal.
(6) Set IR image to zero if corresponding UV image pixel is less than 3 standard deviations above the mean clear water signal.
(7) Create an IR display image spanning 0 to 1 K or 0 to 2 K (black to white).
(8) Subtract IR image from UV image and assign to blue and green display channels.
(9) Assign IR image to red display channel.

The first step relies on the fact that thin oil areas we want to emphasize using the UV channel are always bright, positive contrast features. For the Neah Bay conditions (clear), the scaling indicated gave good definition of oil structure while allowing isolated glints to saturate. The erosion operator (step 2) did a good job removing most isolated glints, aiding the cosmetic appearance of the composites without seriously affecting the identity of oiled areas. A three by three square erosion operator was used; the erosion operator replaces the value of the target pixel by the minimum value contained in the surrounding eight pixels.

The IR image is inverted so that brighter tones in the composite correspond to a more negative IR contrast; for the amount of oil at Neah Bay, this is believed to always correspond to thicker oil. Zeroing the IR image based on UV signature levels (step 6) proved useful in the Neah Bay data to reduce the impact of thermal scars on the composite. At Neah Bay, the oil always produced a positive UV signature contrast relative to the water, so this technique was successful. This will not always be the case, nor will the IR signature always be negative contrast and monotonically related to slick thickness (e.g., thicker slicks under sunlit conditions will tend to provide a positive contrast IR signature). Nevertheless, the UV/IR composite appears to be very effective in summarizing relevant information contained in the individual band images.

FORTHCOMING ARTICLES

Richard Aspinall and *Neil Veitch*, Habitat Mapping from Satellite Imagery and Wildlife Survey Data Using a Bayesian Modeling Procedure in a GIS.

David G. Barber, Mohammed E. Shokr, Richard A. Fernandes, Eric D. Soulis, Dean G. Flett, and *Ellsworth F. LeDrew*, A Comparison of Second-Order Classifiers for SAR Sea Ice Discrimination.

Russell G. Congalton, Kass Green, and *John Teply*, Mapping Old Growth Forests on National Forest and Park Lands in the Pacific Northwest from Remotely Sensed Data.

Russell G. Congalton and *Kass Green*, A Practical Look at the Sources of Confusion in Error Matrix Generation.

Jean-Pierre Djamdji, Albert Bijaoui, and *Roger Maniere*, Geometrical Registration of Images: The Multiresolution Approach.

John R. Dymond, An Improved Skidmore/Turner Classifier.

Maria Fiorella and *William J. Ripple*, Analysis of Conifer Forest Regeneration Using Landsat Thematic Mapper Data.

Douglas G. Goodin, Luoheng Han, Rolland N. Fraser, Donald C. Rundquist, Wesley A. Stebbins and *John F. Schalles*, Analysis of Suspended Solids in Water Using Remotely Sensed High Resolution Derivative Spectra.

Linda H. Graff and *E. Lynn Usery*, Automated Classification of Generic Terrain Features in Digital Elevation Models.

Edwin J. Green, William E. Strawderman, and *Teuvo M. Airola*, Assessing Classification Probabilities for Thematic Maps.

John R. Jensen, Sunil Narumalani, Oliver Weatherbee, and *Halkard E. Mackey, Jr.*, Measurement of Seasonal and Yearly Cattail and Waterlily Changes Using Multidate SPOT Panchromatic Data.

Chris L. Lauver and *Jerry L. Whistler*, A Hierarchical Classification of Landsat TM Imagery to Identify Natural Grassland Areas and Rare Species Habitat.

Oğuz Müftoğlu, A Data Reduction Approach Using the Collinearity Model from Non-Metric Photography.

M. Nazim, SOM Equations with Modifications to Estimate Longitude from Ascending Node, and Constants for the Clarke and Everest Spheroids.

Scott A. Samson, Two Indices to Characterize Temporal Patterns in the Spectral Response of Vegetation.

Paul A. Sorensen and *David P. Lanter*, Two Algorithms for Determining Partial Visibility and Reducing Data Structure Induced Error in Viewshed Analysis.

I. Tannous and *B. Pikeroen*, Parametric Modeling of Spaceborne SAR Image Geometry Application: SEASAT/SPOT Image Registration.

Gregory S. Tudor and *Larry J. Subarbaker*, GIS Orthographic Digitizing of Aerial Photographs by Terrain Modeling.

Yong-Jian Zheng, Digital Photogrammetric Inversion: Theory and Application to Surface Reconstruction.